Influence of flooding underneath the Amazon rainforest on Sentinel-1 backscatter

10.36227/techrxiv.23523930.v1

Influence of flooding underneath the Amazon rainforest on Sentinel-1 backscatter

Felix Cremer*, Nora Linscheid *, Miguel D. Mahecha †‡, Mikhail Urbazaev §, John Truckenbrodt ¶, Antje Uhde ‖ *, Christiane Schmullius ‖ and Christian Thiel **
* Max Planck Institute for Biogeochemistry, 07745 Jena, Germany
† Remote Sensing Center for Earth System Research, Leipzig University, 04103 Leipzig, Germany ‡Helmholtz Centre for Environmental Research, 04318 Leipzig, Germany §Department of Geographical Sciences, University of Maryland, College Park, MD 20742, USA ¶ German Aerospace Center, German Remote Sensing Data Center, 82234 Wessling, Germany ‖ Chair of Earth Observation, Friedrich Schiller University, 07743 Jena, Germany
**German Aerospace Center, Institute of Data Science, 07743 Jena, Germany

Abstract

It is widely assumed that C-Band Synthetic Aperture Radar (SAR) signal do not reach the forest floor in dense forests, and that hence C-Band SAR cannot be used for sub-canopy flood mapping in tropical forests. Indeed, flooded and non-flooded forests are not distinguishable in single C-Band acquisitions. The question is whether long-term seasonal dynamics in C-Band SAR time series data encode flooding dynamics underneath the canopy. In this paper we investigate the relationship of Sentinel-1 backscatter with sub-canopy flooding in the Amazon rain forest. We use the Empirical Mode Decomposition to extract annual modes in the backscatter signal and use the correlation to the water level of a nearby river to understand the dynamics of the Sentinel-1 signal. Clusters of these correlations coincide well with known forest flooding areas in the VH signal. The analysis shows that the Sentinel-1 C-Band backscatter is influenced by floodings underneath the canopy in the Amazon rain forest. The presented approach could allow to systematically map flooded areas throughout tropical rain forests.

I. Introduction

The lower Amazon basin floodplain forests are dominated by an annual flood pulse from the Andes to the Atlantic ocean which leads to large floodings under the forest [1]. L-Band Synthetic Aperture Radar (SAR) is suitable for detecting these floodings even in single acquisitions [2] due to its longer wavelength penetrating through forest canopy. Flooding is assumed not to influence the C-Band SAR backscatter signal and has been shown to be temporally invariant over tropical rain forest in copolarized RADARSAT-1 and ERS-1/2 data [3]. These results have been confirmed by radiative transfer models but they assumed that the cross-polarized data is influenced by changes in the canopy only [4]. Consequently, the Amazon rain forest is assumed to appear as a homogeneous scatterer for the calibration and validation of C-Band SAR systems [5], [6], [7]. With Sentinel-1 we now have time series in high spatial resolution based on C-Band SAR, both in co- and cross-polarisation.

Flooded Forest Mapping with Radar in the Amazon

According to the literature review by Tsygantskaya et al. [8] on flooded vegetation mapping with SAR, the majority of studies use single time steps. A broad consensus is that only longer wavelengths like L-Band or P-Band are able to penetrate the dense forest canopy of the Amazon rainforest to induce a double bounce between tree trunks and water surface [9], [10], [11], [12]. According to several references, C-Band data, instead, should only be used for flooded forest mapping in sparse vegetation and leaf-off situations [13], [2]. Therefore, flooded forest mapping studies in the Amazon Basin have indeed mostly used L-Band SAR data [14], and L-Band HH has worked best for detecting flooded Amazon rainforest [15], [16].

Flooded Forest Mapping with C-Band SAR

So far, C-Band SAR backscatter has been used to detect flooding under sparse temperate forests [17], [18], [19]. According to Townsend et al. 2002 [19] the detection of flooded forests depends only on the basal area and the height to the bottom of the canopy and not on other forest structure parameters like the canopy density or the leaf area index. Haarpaintner and Hindberg (2019) [20] compared L-Band and C-Band data for the classification of different wetland classes and found that L-Band is better suited for the delineation of flooded forest, but they suggested that the dense time series of C-Band SAR backscatter may compensate for the shallower vegetation penetration depth. Slagter et al. [21] used multi-temporal statistics to map different wetland classes - but they were not able to map flooded forests and stated that more sophisticated time series methods are needed for the analysis of Sentinel-1 time series.

Schlaffer et al. [22] analysed a time series of Envisat ASAR backscatter signals of 100 time steps over two years to map wetland classes and soil moisture dynamics. They distinguished between permanent water, seasonally flooded, permanent flooded vegetation, seasonally flooded vegetation and land. For this classification they decomposed the time series into subsignals with different temporal frequencies using

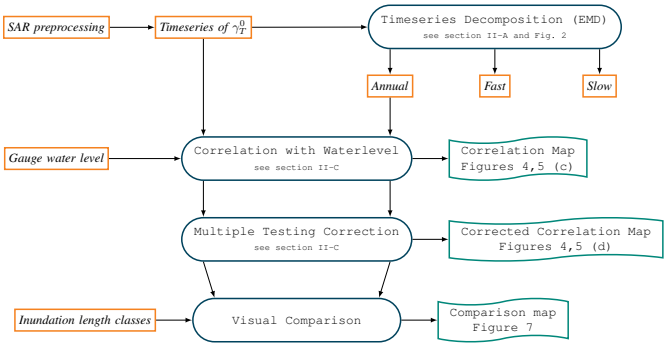

Fig. 1. Workflow of this paper. First we produced a preprocessed Sentinel-1 backscatter time series from GRD data. This time series has been decomposed into fast, annual and trend components. For the further analysis we only used the annual frequency component. Then we correlated the time series of every pixel against the time series of a gauge level at the nearby river as a flood seasonality proxy.

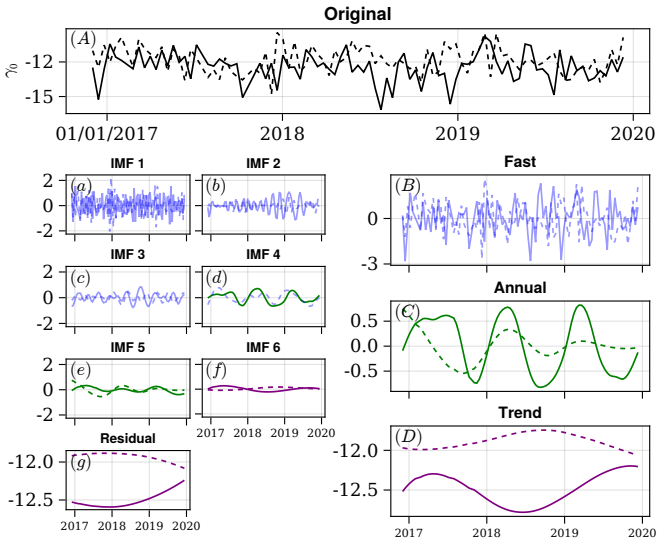

Fig. 2. Frequency binning of the Intrinsic Mode Functions into Fast, Annual and Trend bins for two example time series. The annual signal might be in different IMFs, therefore we perform the frequency binning. The derived IMFs are on the left and are coloured according to their frequency classification. Identically coloured time series on the left side are summed together to compute the signals on the right. The sum of the different frequency signals (B), (C) and (D) return the original signal (A).

Fourier analysis. They found a clear seasonality due to flooding only for non-vegetated or sparsely vegetated land cover classes.

In summary, while C-Band SAR data has been used for flood mapping under temperate forests, its application for forest flood mapping in the tropics is rarely explored. Time series analysis using decomposition has shown to be a promising approach to derive seasonality from SAR data [22].

In this study we hypothesize that C-Band SAR data is not homogeneous in space and time over seasonally flooded Amazon forests, and that flooding patterns can be properly retrieved from Sentinel-1 time series. However, like [22] we also assume that a decomposition into discrete temporal frequencies is needed to extract the dynamics of interest, which otherwise might be hidden in a low signal-to-noise ratio. However, it has also been suggested that highly data adaptive decomposition methods shall be preferred for satellite remote sensing applications in order to address non-linearities in the underlying dynamics [23]. One relevant approach is Empirical Mode Decomposition (EMD)[24], a fully data driven alternative to the Fourier transform. EMD is able to identify subsignals even in the presence of changing amplitudes and frequencies, allowing to summarize complex temporal dynamics in a few components. In this study, we compare seasonal signals identified via EMD in Sentinel-1 data with the water levels of a nearby river to test whether flooding-induced signal seasonality can be identified. Our aim is to understand how well this approach distinguishes seasonally flooded from non-flooded forests compared to using the original signal.

II. Methods

In this paper we analyse time series of Sentinel-1 Ground Range Detected (GRD) data. We first preprocessed the data to radiometrically terrain corrected gamma naught (γ^0_T) time series (see section III-B for details). Then we decomposed the backscatter time series using Empirical Mode Decomposition (EMD) (section II-A) into three sub signals with a high (sub-seasonal), annual, and low (inter-annual) temporal frequency (section II-B). We correlate seasonal sub signals with river water level data over known areas of seasonally flooded and non-flooded forests to determine whether extracted signatures can capture flooding seasonality. See Figure 1 for an overview of the workflow of this paper.

A. Empirical Mode Decomposition

We applied the Empirical Mode Decomposition (EMD) [24] to decompose the backscatter time series into subsignals. This method has been previously used to filter unwanted effects from both optical remote sensing data [25], [26], but also from C-Band SAR data [27], [28]. EMD is an alternative to the Fourier transform without having to set an a priori base for the decomposition. EMD works via sifting the signal by selecting the dominant mode. To do that we follow these steps:

1) Find the local extrema
2) Interpolate a smooth function through the local minima and maxima respectively.
3) Compute the average of these two interpolations. This is the mean of the envelope.
4) Subtract this mean envelope from the original signal.
5) Repeat the first four steps with the residual of the subtraction. These siftings are done until either the mean envelope is zero or the number of local maxima and minima differ at most by one and is fix for multiple iteration steps.

The resulting time series is called an intrinsic mode function (IMF) and we can subtract this from the original data and repeat the sifting process. By doing that we decompose the signal into multiple IMFs. Figure 2 (a-g) show the IMFs for two example time series. The IMFs have the following properties:

1) the number of local maxima and zero crossings differ at most by one
2) the local maxima are positive
3) the local minima are negative.

The IMFs are ordered by temporal frequency in descending order. The IMFs do not have to be physically meaningful by themselves [24], as the decomposition could be too finely grained or the resulting IMFs could be a mixture of multiple frequencies. To combine all IMFs containing seasonal information into one seasonal subsignal, next we applied a frequency binning approach.

B. Frequency Binning

We implement a frequency binning approach to derive fast, annual and trend subsignals of our Sentinel-1 time series data. To classify the frequency of an IMF we first detect the local maxima. Then we compute the time spans between subsequent local maxima. We sort these time spans into bins by selecting every signal which has a time span of 295 to 435 days as annual signals. Every shorter span is classified as fast and every longer span is classified as trend. We then classify the IMF as either fast, annual, or trend according to the maximal number of classifications of the distance between local extrema. The final fast, annual and trend time series are the sum of the so classified IMFs. For most pixels, IMF 5 represents the annual frequency but for some pixels this IMF is classified as a slow moving trend signal, see figure 2 for the frequency binning of two example time series.

C. Correlation Analysis

To analyse the relationship between the Sentinel-1 SAR signal and the flooded forest, we compute the pearson correlation between the water level of the nearby river and the time series signal. The flood occurrence in the surrounding forests is driven by the water height of the river. Therefore, this correlation can be interpreted as a proxy for the seasonality of the SAR signal which is concurrent with the seasonality of the flood occurrence.

We test the significance of the correlation with a p-value of 0.05. Because we have more than 45 million time series, we control for this multiple testing following the methodology proposed by Cortés et al. (2021) [29]. This ensures that the probability of observing one false positive in all of our results is limited to 5%. The method is permutation based, and we use the block shuffle method (block size = 7) of the *TimeseriesSurrogates.jl* package [30] to generate permutations with similar temporal autocorrelation of the water gauge level data.

III. Test site and Data sets

A. Test site

The test site is located at the *Juruá* river, a southern tributary of the Amazon main stem. The region has a mean annual precipitation of $3679\,\mathrm{mm}$ measured over a three year period (2008 to 2010) [31] and a mean annual temperature of $27\,^{\circ}\mathrm{C}$.

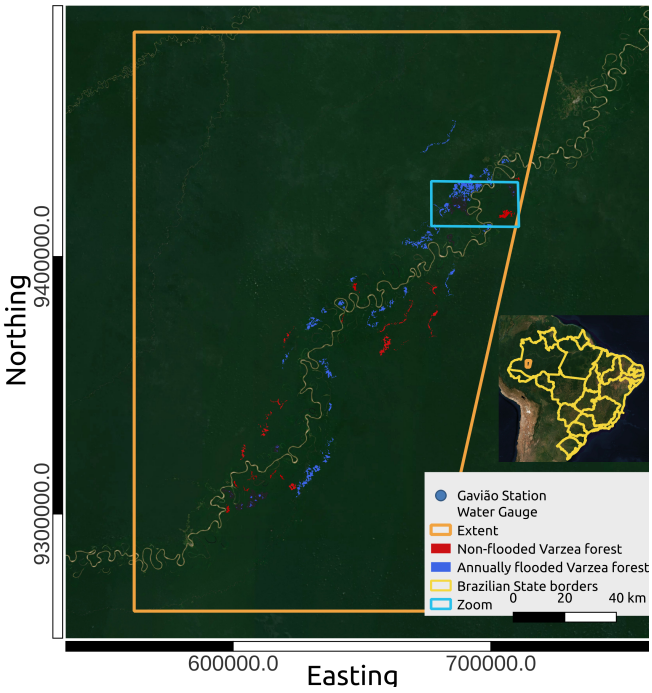

Fig. 3. Area of interest at the *Juruá* river. The flooding references have been generated from L-Band acquisitions. Background Image: MapTiler Satellite. Reserva Extrativista do Medio *Juruá* © Openstreetmap contributors.

The rainy season lasts from November to April and the non-rainy season from May to October. The humidity ranges from $92\,\%$ to $98\,\%$ and peaks from January to April. The *Juruá* river is subject to an annual mono-modal flood pulse, which originates in the Andes. The flood pulse is asynchronous to the precipitation and begins six weeks after the start of the rainy season. The water level varies by $15\,\mathrm{m}$ between high and low water in normal conditions and the peak is reached three weeks after the start of the flood pulse. The elevation of the region ranges from $65\,\mathrm{m}$ to $170\,\mathrm{m}$ above sea level. For smaller tributaries of the *Juruá* the flooding is driven by local precipitation. This leads to less predictable flooding patterns [31]. At certain water levels, the overflow of levees can lead to rapid flooding of cut-off lakes and depressions in the flood plain.

In this study we differentiate between floodplain forests and the non-flooded upland forest (*terra firme*). The floodplain forest and the terra firme forest both have low levels of leaf fall and leaf flush throughout the year with a marked seasonality. The leaf fall peaked in both forest types in March to April and leaf flush peaked in March in floodplain forests, but was temporally more stable in terra firme. Floodplain forest has a higher amount of fine woody litter - like twigs, branches and bark - in the leaf traps compared to terra firme forest. Peaks in leaflessness - when one to two percent of the trees are leafless - occur in June for the floodplain forest and in September in terra firme forests [31].

B. Sentinel-1 Data

We processed the Sentinel-1 data with the workflow described in [32] as implemented in the pyroSAR python package

[33]. The preprocessing includes thermal noise and border noise removal, calibration, multilooking, radiometric terrain correction and geocoding to a $30\,\mathrm{m}$ pixel spacing. We use a stack of 100 Sentinel-1 acquisitions from October 2016 until February 2020 from the descending orbit number 127. The acquisitions have a temporal resolution of 12 days with a few gaps in the time series.

C. Reference Data

As reference for the flooding occurrence we use a land cover map based on 12 PALSAR ScanSAR acquisitions from 2006 to 2009 with $100\,\mathrm{m}$ pixel spacing [34]. The map was produced at $30\,\mathrm{m}$ pixel size. To avoid mixed backscattering contributions from different classes and to address potential geolocation inaccuracies, we use only inner polygons with a buffer size of 90 meters. The classification distinguishes between floodplain forests with different flooding period lengths and terra firme as well as open water areas and non-forest areas. The map covers the main floodplain and the two tributaries from the south. The water level imaged range from $31\,\mathrm{cm}$ to $1458\,\mathrm{cm}$ [34]. For the visual inspection in Figure 7, we use a water inundation duration map produced from a PALSAR-2 (L-Band) HH time-series where flooding timing was combined with the *Gavião* water gauge to determine the mean flood duration [35].

For the water level of the *Juruá* river, which flows through our area of interest, we used the water height information at the *Gavião* station in Carauarí [36]. The water level reaches up to 18 meters above the lowest measurement during the study period. The blue line in Figure 6 shows the water level time series of this station.

IV. Results

To test whether flooding below dense forest canopy can be detected in the Amazon using Sentinel-1 C-Band backscatter time series, we first compare time series of known seasonally flooded and non-flooded regions against the water level of the nearby river. We then analyse, whether the patterns in the averaged time series can also be extracted on the pixel level to differentiate between flooded and non-flooded forests.

Figure 6 shows the time series of spatial averages for the VH and VV data for seasonally flooded and non-flooded forests. In the spatial average of frequently flooded areas there is a seasonality in the Sentinel-1 time series which corresponds to the seasonality of the water level of the nearby river system, which is not visible in the non-flooded forest. This seasonality is more pronounced on the VH data. If such an aggregated pattern emerges, it must be also contained in single pixel time series, even if hardly visible due to very low signal-to-noise ratios.

In the RGB of Sentinel-1 data for different time steps in VH (Figure 4 (a)) and VV (Figure 5 (a)) there are no distinct spatial features visible except for the permanent open water areas in black and the recurrently flooded open areas in red. There seems to be a slight shift in the texture in the VH data (Figure 4) between the southeastern part of the area and the areas closer to the main stem of the river. This texture is more pronounced in the RGB of the temporal mean, 5th and 95th percentile (Figure 4 (b)) but it is not clearly distinguishable.

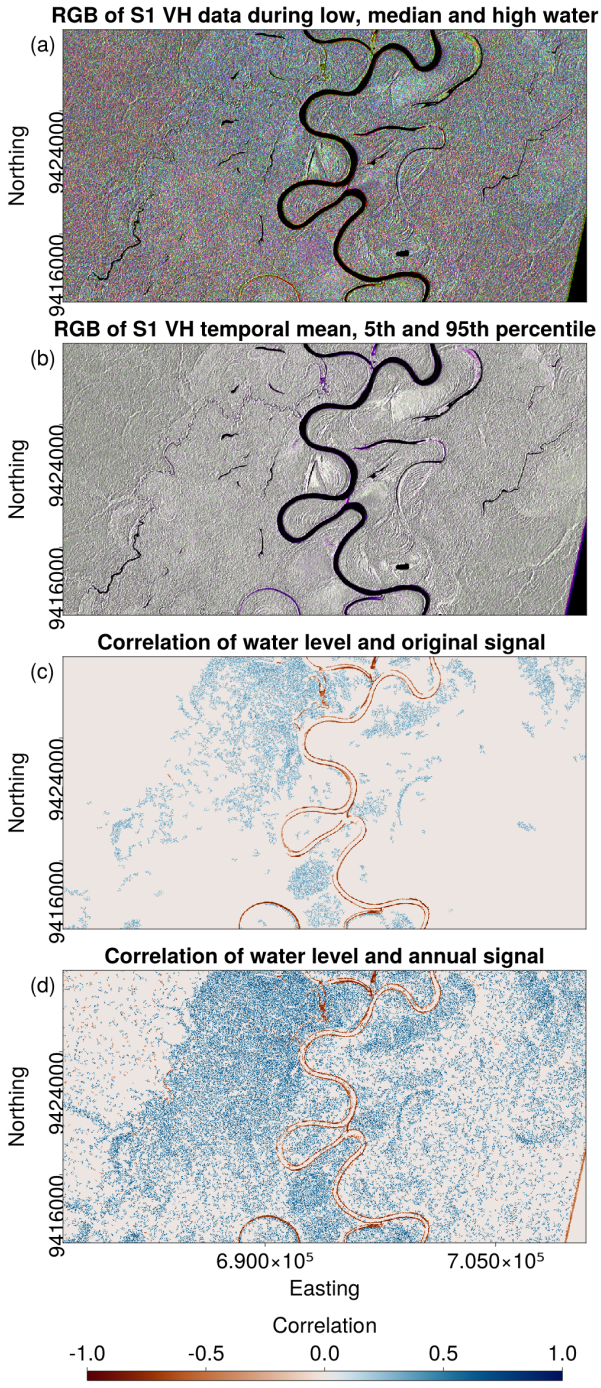

Fig. 4. Comparison of different ways to detect the heterogeneity in the Sentinel-1 VH data. (A): RGB composite of original acquisitions during low, median and high water levels (B): RGB composite of different temporal statistics (C): Correlation of the water level to the original Sentinel-1 VH time series (D): Correlation of the water level to the annual Sentinel-1 VH time series. The colormap represents the color scale of the correlation maps (C) and (D).

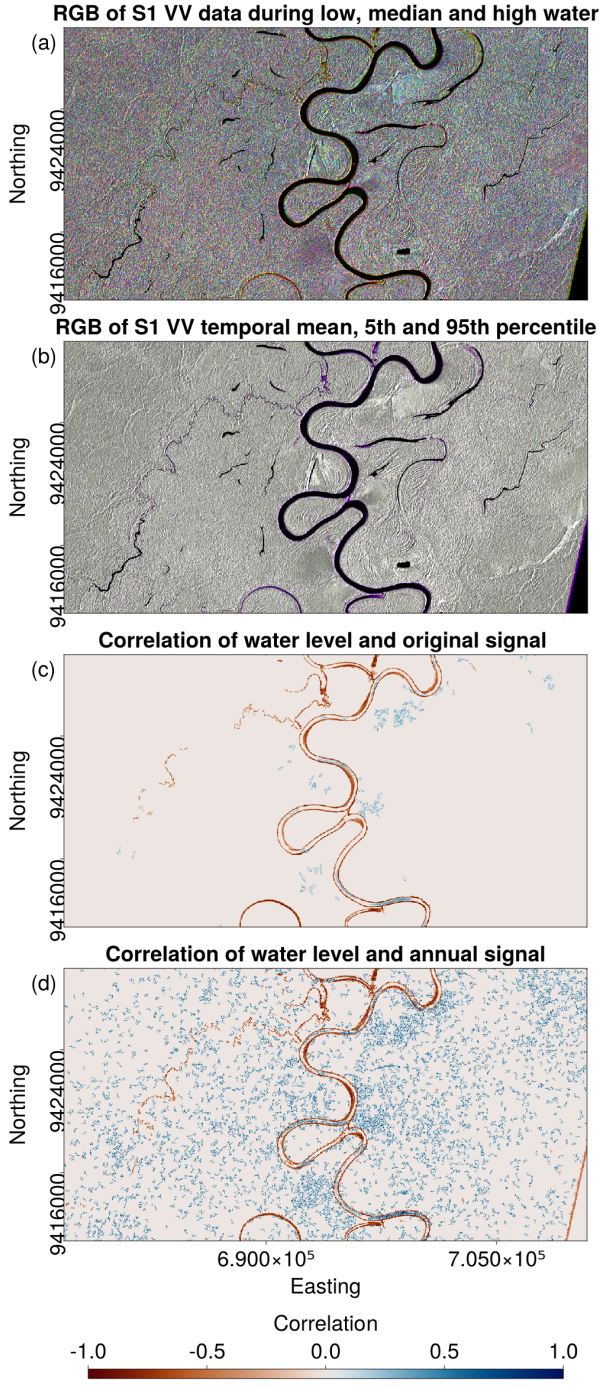

Fig. 5. Comparison of different ways to detect the heterogeneity in the Sentinel-1 VV data. (A): RGB composite of original acquisitions during low, median and high water level (B): RGB composite of different temporal statistics (C): Correlation of the water level to the original Sentinel-1 VV time series (D): Correlation of the water level to the annual Sentinel-1 VV time series. The colormap represents the color scale of the correlation maps (C) and (D).

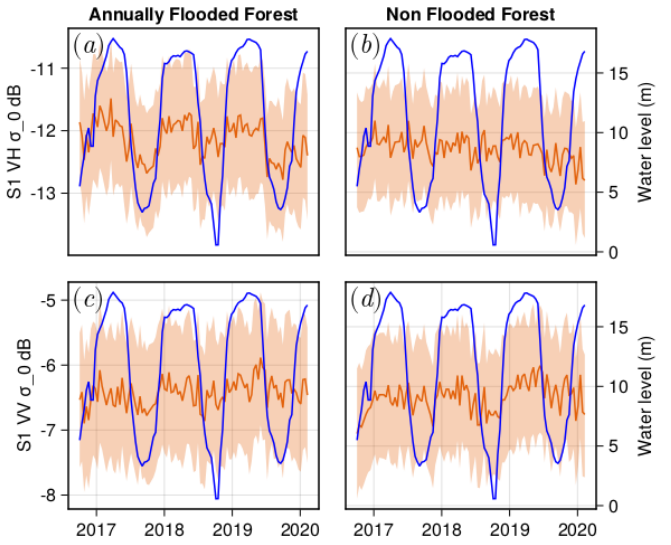

Fig. 6. Temporal box plot comprised of the spatial mean as colored line and the 25th to 75th percentiles as shaded areas example reference areas of seasonally flooded forest (left) and non-flooded forest (right). The blue line depicts the water level at the *Gavião* station. The Sentinel-1 VH (top) time series show a seasonality in the flooded forest which corresponds to the seasonality of the water level. In the Sentinel-1 VV (bottom) time series there is a small seasonality in the spatial mean. The non-flooded forest does not show such seasonality.

A. *Frequency Binning of Sentinel-1 data*

B. *Correlation maps*

Figures 4/5 (c) and (d) illustrate the correlation between the water level and the S1 signal for a small subset of the area of interest. Areas at the edge of the river show a consistent negative correlation to the water level in both polarisations. The VH original signal already shows a distinction of the flooded and non-flooded areas with a low but spatially consistent significant correlation to the water level. In the correlation for the extracted annual VH data the clusters of significant correlation are denser and the correlation values are higher, but there are more random small clusters at the edge of the image. The VV data shows only few areas of positive correlation with the water level in the original data. In the annual signal positive correlated pixels are randomly distributed over the whole image and no clear distinction between flooding regimes is visible. Taken together, flooding regimes are better distinguished in the VH signal.

Figure 7 shows the comparison of the L-Band based inundation length map and the significant correlation between the Sentinel-1 VH annual data and the water level. There is a good agreement between the longer flooded areas and the correlation. The edge between the flooded and non-flooded areas in the north west is also clearly distinguishable in the correlation map.

We show the correlation between the water level and the Sentinel-1 VH annual signal for the whole area of interest in Figure 8. We identify a broad band of high correlation around the river. This is surrounded by areas of sparser significant correlation patterns which are mostly non-flooded forest. In the

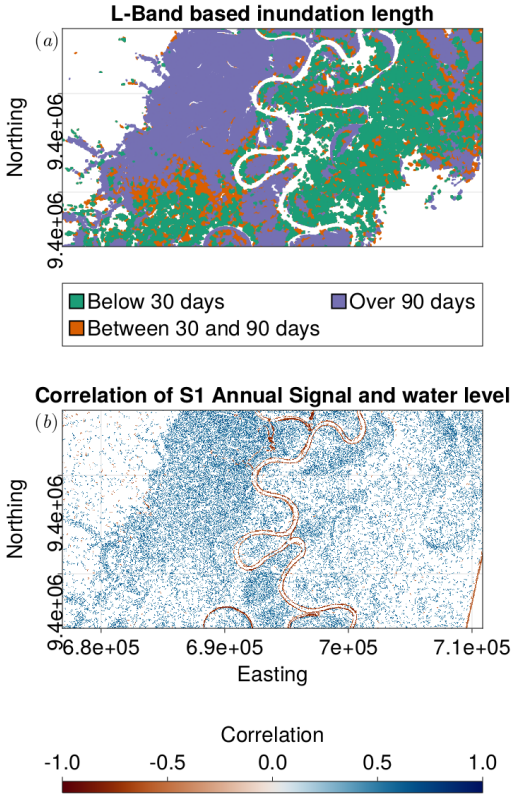

Fig. 7. Classification of the average annual inundation length based on L-Band data (top) [35] Map of the temporal correlation between the gauge water level and the Sentinel-1 VH annual signal (bottom). The positive correlations are clustered near the river and show a generally good overlap with the flooded forests with a yearly inundation length of more than 90 days.

southeast of the area there is some region of higher correlation values in single pixels which is not linked to a nearby river. In the northwest, we see small river bands which are tributaries of the next large river system.

V. Discussion

First, we discuss the differences of the results obtained based on VH and VV data. Second, we discuss the effect of the derived annual signal in the correlation with the water level. Third, we discuss possible explanations for the emerging detection potential of sub-canopy floodings in the C-Band VH data.

One question is why we find denser correlation patterns between the seasonal Sentinel-1 signal with the observed water levels compared to the original data as seen in Figure 4 and 5 (c) and (d). This effect can be partly explained by the denoising of the signal by removing the fast oscillating parts of the original signal, which enhances the underlying seasonality. In fact, small rivers in the northern part of the area of interest are visible in the VH correlation results for the annual signal (Figure 8. However, the denoising also leads to a higher number of false positives which cannot be fully removed by the multiple testing correction leading to the noisy appearance of the correlation map of the annual signal.

The small areas with large negative correlation in the middle of figures 4 and 5 (c) and (d) are pixels of open areas near the river which are flooded during high water and therefore have a drop in backscatter. These areas are also visible in the RGB of the original data as small reddish lines at the river edge and as purple in the multi temporal statistics. The visibility in the RGB maps implies a huge change in backscatter between flooded and non-flooded states (Figure 4 and 5 (a).

We see a clear difference in the correlation to the water level for seasonally flooded compared to non-flooded forest areas in the Sentinel-1 VH but not in the VV signal. In the VH signal there are clusters around the river of high correlation to the water level which indicate that these high correlations are coming from the common driver of being flooded. The correlation results in VH (Figure 7) (show very similar edges as the reference areas which have been retrieved from PALSAR-2 L-Band data. In the VV signal these clusters are not visible (Figure 5. Therefore, the backscatter behaviour of flooded forest is different to the forest in the non-flooded state in the VH signal. The correlation with the water level of the *Juruá* river can be interpreted as an indicator for seasonality, because the water level has a yearly seasonality.

We see two possible explanations for this higher seasonality in the VH data in flooded forests. Either a direct interaction of the radar signal with the water surface beneath the canopy or an indirect effect induced by the flooding. The first explanation could be that the VH signal increases during flooding due to a double bounce between the stems and the water surface, which is then depolarized on the way back through the canopy. This would be a direct measurement of the flooded state and would indicate that the water surface is reached by the C-Band signal. There is a relationship between C-Band HH data and inundation under the forest and unexpectedly forest structure parameters like leaf area index, canopy height and canopy closure did not show a statistically significant influence on this relationship [37]. A second explanation could be that the standing water underneath the canopy might change the water content in the canopy. Possible drivers might be transpiration, and therefore a higher water pressure in the leaves, or higher evaporation from the water below the canopy which is then captured on the leaves. There could also be a structural change in the canopy density during the flooding period. There is only a small seasonality of the leaves in the dominant tree species [31], which should not be high enough to explain the changes in the SAR signal.

VI. Conclusion and Outlook

Our analysis revealed seasonality in cross-polarized Sentinel-1 data over floodplain forests in the Amazon. This is in contrast to the use of the Amazon rainforest as an homogeneous scattering area with medium backscatter intensity for the calibration and validation of C-Band SAR data [38], [6]. It is therefore advisable to check how much this spatiotemporal heterogeneity would influence the calibration and validation results over the Amazon rain forest. These results affirm that for validation and calibration studies for cross polarized C-

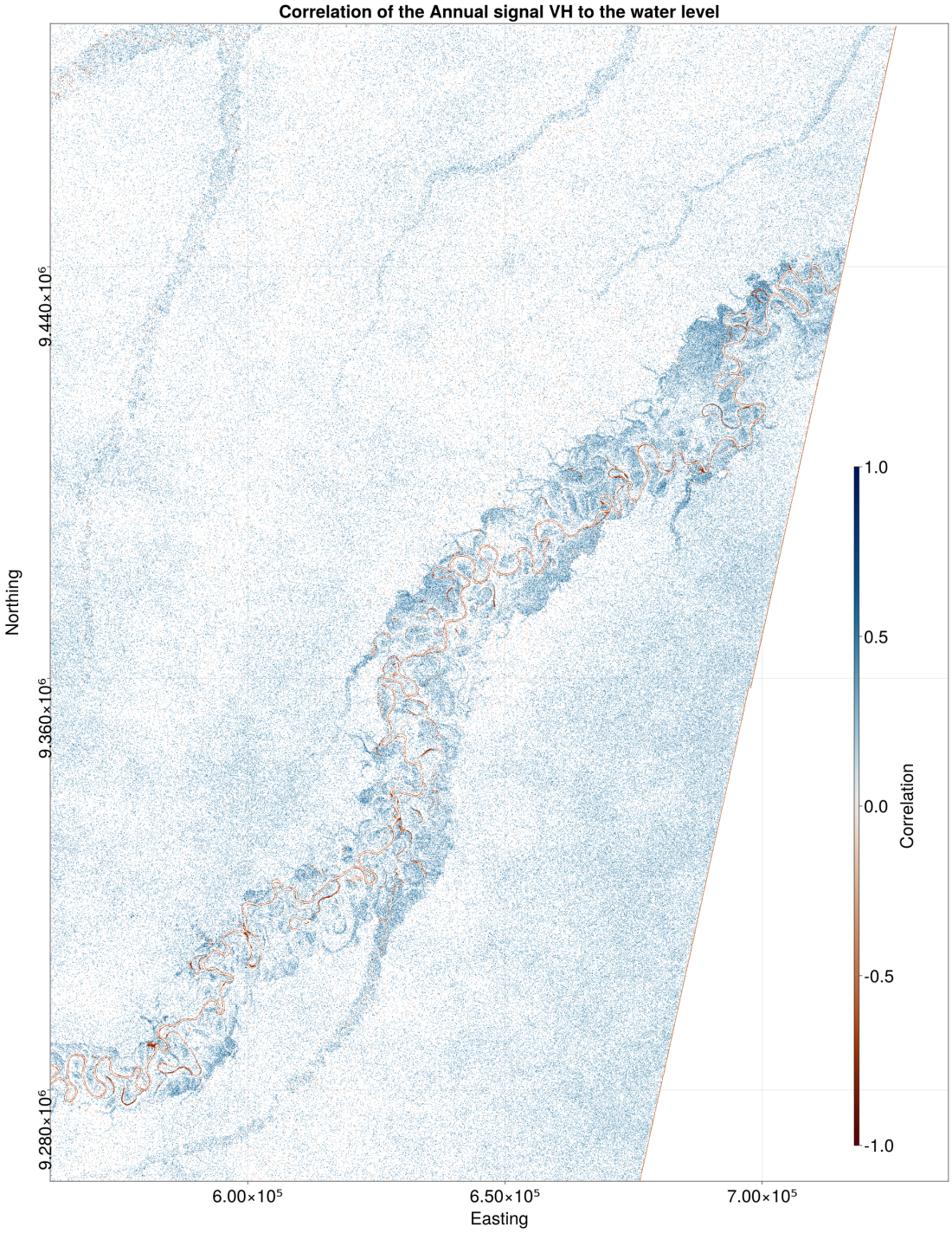

Fig. 8. Correlation between the gauge water level and the annual Sentinel-1 VH signal for the whole area of interest after applying the multiple testing correction. The river is surrounded by a distinct band of higher correlation values. The open water areas near the river are visible as negative correlations. Except for the open water areas, the whole area is covered in dense tropical rain forest.

Band data such as Schmidt et al. (2020)[5], it is advantageous to circumvent the use of larger river systems.

This study furthermore illustrates the possibility of detecting flooding events in the presence of dense forest canopy using Sentinel-1 C-Band backscatter time series. For further development of a flooded forest mapping product from Sentinel-1 time series, it would be valuable to employ clustering and texture analysis methods. Further research is also needed to explain in detail the source of the seasonality in the Sentinel-1 VH time series. This would require e.g. in situ measurements of the water content inside the canopy and measurements of the structural parameters of the canopy to refute the indirect explanation of the influence of the flooding on the Sentinel-1 backscatter time series.

Acknowledgements

This work uses Copernicus Sentinel data 2017-2020. This work was supported in part by DLR in the Sentinel4REDD project under Grant FKZ:50EE1540 and by DFG in the HyperSense project under Grant TH 1435/4-1. M.U. and A.U. were supported in part by the 2017–2018 Belmont Forum and BiodivERsA joint call for research proposals, under the BiodivScen ERANet COFUND program, and in part by the funding organization of the German Federal Ministry of Education and Research (BMBF) under grant no. 16LC1808A.

Software

The analysis of this paper has been done in the Julia programming language [39]. We used the YAXArrays.jl package for the handling of the raster data cube [40] and the Figure 3 has been set in QGIS [41] and Figures 2 to 8 have been plotted in Makie.jl [42].

References

[1] W. J. Junk, M. T. F. Piedade, J. Schöngart, M. Cohn-Haft, J. M. Adeney, and F. Wittmann, "A classification of major naturally-occurring amazonian lowland wetlands," *Wetlands*, vol. 31, no. 4, pp. 623–640, Aug. 2011.

[2] L. Hess, J. Melack, S. Filoso, and Yong Wang, "Delineation of inundated area and vegetation along the Amazon floodplain with the SIR-C synthetic aperture radar," *IEEE Transactions on Geoscience and Remote Sensing*, vol. 33, no. 4, pp. 896–904, Jul. 1995.

[3] R. Hawkins, E. Attema, R. Crapolicchio, P. Lecomte, J. Closa, P. J. Meadows, and S. K. Srivastava, "Stability of amazon backscatter at C-band: Spaceborne results from ERS-1/2 and RADARSAT-1." vol. 450, p. 99, Mar. 2000.

[4] Y. Wang, L. L. Hess, S. Filoso, and J. M. Melack, "Understanding the radar backscattering from flooded and nonflooded Amazonian forests: Results from canopy backscatter modeling," *Remote Sensing of Environment*, vol. 54, no. 3, pp. 324–332, Dec. 1995.

[5] K. Schmidt, M. Schwerdt, N. Miranda, and J. Reimann, "Radiometric Comparison within the Sentinel-1 SAR Constellation over a Wide Backscatter Range," *Remote Sensing*, vol. 12, no. 5, p. 854, Mar. 2020.

[6] A. P. Luscombe, "RADARSAT-2 SAR image quality and calibration operations," *Canadian Journal of Remote Sensing*, vol. 30, no. 3, p. 10, 2004.

[7] G. Sun, Z. Li, L. Huang, Q. Chen, and P. Zhang, "Quality analysis and improvement of polarimetric synthetic aperture radar (SAR) images from the GaoFen-3 satellite using the Amazon rainforest as an example," *International Journal of Remote Sensing*, vol. 42, no. 6, pp. 2131–2154, Mar. 2021.

[8] V. Tsyganskaya, S. Martinis, P. Marzahn, and R. Ludwig, "SAR-based detection of flooded vegetation – a review of characteristics and approaches," *International Journal of Remote Sensing*, vol. 39, no. 8, pp. 2255–2293, Apr. 2018.

[9] H. Lee, T. Yuan, H. Yu, and H. C. Jung, "Interferometric SAR for Wetland Hydrology: An Overview of Methods, Challenges, and Trends," *IEEE Geoscience and Remote Sensing Magazine*, vol. 8, no. 1, pp. 120–135, Mar. 2020.

[10] C. Palmann, S. Mavromatis, M. Hernandez, J. Sequeira, and B. Brisco, "Earth observation using radar data: An overview of applications and challenges," *International Journal of Digital Earth*, vol. 1, no. 2, pp. 171–195, Jun. 2008.

[11] F. Papa and F. Frappart, "Surface Water Storage in Rivers and Wetlands Derived from Satellite Observations: A Review of Current Advances and Future Opportunities for Hydrological Sciences," *Remote Sensing*, vol. 13, no. 20, p. 4162, Oct. 2021.

[12] J. Ferreira-Ferreira, T. S. F. Silva, A. S. Streher, A. G. Affonso, L. F. de Almeida Furtado, B. R. Forsberg, J. Valsecchi, H. L. Queiroz, and E. M. L. de Moraes Novo, "Combining ALOS/PALSAR derived vegetation structure and inundation patterns to characterize major vegetation types in the Mamirauá Sustainable Development Reserve, Central Amazon floodplain, Brazil," *Wetlands Ecology and Management*, vol. 23, no. 1, pp. 41–59, Feb. 2015.

[13] S. Plank, M. Jüssi, S. Martinis, and A. Twele, "Mapping of flooded vegetation by means of polarimetric Sentinel-1 and ALOS-2/PALSAR-2 imagery," *International Journal of Remote Sensing*, vol. 38, no. 13, pp. 3831–3850, Jul. 2017.

[14] A. C. Fassoni-Andrade, A. S. Fleischmann, F. Papa, R. C. D. de Paiva, S. Wongchuig, J. M. Melack, A. A. Moreira, A. Paris, A. Ruhoff, C. Barbosa, D. A. Maciel, E. Novo, F. Durand, F. Frappart, F. Aires, G. M. Abrahão, J. Ferreira-Ferreira, J. C. Espinoza, L. Laipelt, M. H. Costa, R. Espinoza-Villar, S. Calmant, and V. Pellet, "Amazon Hydrology From Space: Scientific Advances and Future Challenges," *Reviews of Geophysics*, vol. 59, no. 4, Dec. 2021.

[15] J. Rosenqvist, A. Rosenqvist, K. Jensen, and K. McDonald, "Mapping of maximum and minimum inundation extents in the amazon basin 2014–2017 with ALOS-2 PALSAR-2 ScanSAR time-series data," *Remote Sensing*, vol. 12, no. 88, p. 1326, Jan. 2020.

[16] A. Fleischmann, F. Papa, A. Fassoni-Andrade, J. M. Melack, S. Wongchuig, R. C. Dias De Paiva, S. K. Hamilton, E. Fluet-Chouinard, R. Barbedo, F. Aires, and e. al., "How much inundation occurs in the Amazon River basin?" *Earth and Space Science Open Archive*, p. 67, 2021.

[17] P. Kandus, H. Karszenbaum, T. Pultz, G. Parmuchi, and J. Bava, "Influence of Flood Conditions and Vegetation Status on the Radar Backscatter of Wetland Ecosystems," *Canadian Journal of Remote Sensing*, vol. 27, no. 6, pp. 651–662, Dec. 2001.

[18] M. W. Lang, E. S. Kasischke, S. D. Prince, and K. W. Pittman, "Assessment of C-band synthetic aperture radar data for mapping and monitoring Coastal Plain forested wetlands in the Mid-Atlantic Region, U.S.A." *Remote Sensing of Environment*, vol. 112, no. 11, pp. 4120–4130, Nov. 2008.

[19] P. A. Townsend, "Mapping Seasonal Flooding in Forested Wetlands Using Multi-Temporal Radarsat SAR," *Photogrammetric Engineering & Remote Sensing*, p. 8, 2001.

[20] J. Haarpaintner and H. Hindberg, "Multi-temporal and multi-frequency SAR analysis for forest land cover mapping of the mai-ndombe district (democratic republic of congo)," *Remote Sensing*, vol. 11, no. 24, p. 2999, Dec. 2019.

[21] B. Slagter, N.-E. Tsendbazar, A. Vollrath, and J. Reiche, "Mapping wetland characteristics using temporally dense Sentinel-1 and Sentinel-2 data: A case study in the St. Lucia wetlands, South Africa," *International Journal of Applied Earth Observation and Geoinformation*, vol. 86, p. 102009, Apr. 2020.

[22] S. Schlaffer, M. Chini, D. Dettmering, and W. Wagner, "Mapping Wetlands in Zambia Using Seasonal Backscatter Signatures Derived from ENVISAT ASAR Time Series," *Remote Sensing*, vol. 8, no. 5, p. 402, May 2016.

[23] M. D. Mahecha, L. M. Fürst, N. Gobron, and H. Lange, "Identifying multiple spatiotemporal patterns: A refined view on terrestrial photosynthetic activity," *Pattern Recognition Letters*, vol. 31, no. 14, pp. 2309–2317, 2010.

[24] N. E. Huang, Z. Shen, S. R. Long, M. C. Wu, H. H. Shih, Q. Zheng, N.-C. Yen, C. C. Tung, and H. H. Liu, "The empirical mode decomposition and the Hilbert spectrum for nonlinear and non-stationary time series analysis," *Proceedings of the Royal Society of London. Series A: Mathematical, Physical and Engineering Sciences*, vol. 454, no. 1971, pp. 903–995, Mar. 1998.

[25] R. Verma and S. Dutta, "Vegetation dynamics from denoised NDVI using empirical mode decomposition," *Journal of the Indian Society of Remote Sensing*, vol. 41, no. 3, pp. 555–566, Sep. 2013.

[26] Y.-l. Kong, Y. Meng, W. Li, A.-z. Yue, and Y. Yuan, "Satellite image time series decomposition based on EEMD," *Remote Sensing*, vol. 7, no. 1111, pp. 15 583–15 604, Nov. 2015.

[27] F. Cremer, M. Urbazaev, C. Berger, M. D. Mahecha, C. Schmullius, and C. Thiel, "An image transform based on temporal decomposition," *IEEE Geoscience and Remote Sensing Letters*, vol. 15, no. 4, pp. 537–541, Apr. 2018.

[28] F. Li, D. Hu, C. Ding, and W. Zhang, "InSAR phase noise reduction based on empirical mode decomposition," *IEEE Geoscience and Remote Sensing Letters*, vol. 10, no. 5, pp. 1180–1184, Sep. 2013.

[29] J. Cortés, M. Mahecha, M. Reichstein, and A. Brenning, "Accounting for multiple testing in the analysis of spatio-temporal environmental data," *Environmental and Ecological Statistics*, vol. 27, Jun. 2020.

[30] K. A. Haaga and G. Datseris, "TimeseriesSurrogates.jl: A Julia package for generating surrogate data," *Journal of Open Source Software*, vol. 7, no. 77, p. 4414, Sep. 2022.

[31] J. E. Hawes and C. A. Peres, "Patterns of plant phenology in Amazonian seasonally flooded and unflooded forests," *Biotropica*, vol. 48, no. 4, pp. 465–475, Jul. 2016.

[32] J. Truckenbrodt, T. Freemantle, C. Williams, T. Jones, D. Small, C. Dubois, C. Thiel, C. Rossi, A. Syriou, and G. Giuliani, "Towards Sentinel-1 SAR Analysis-Ready Data: A Best Practices Assessment on Preparing Backscatter Data for the Cube," *Data*, vol. 4, no. 3, p. 93, Jul. 2019.

[33] J. Truckenbrodt, F. Cremer, I. Baris, and J. Eberle, "PyroSAR: A Framework for large scale SAR satellite data processing," in *Proceedings of 2019 Big Data from Space (BiDS'19): 19 21 February 2019, Munich (Germany).*, P. Soille, S. Loekken, and S. Albani, Eds. LU: Publications Office, 2019, pp. 197–200.

[34] J. E. Hawes, "Landscape-scale variation in structure and biomass of Amazonian seasonally flooded and unflooded forests," *Forest Ecology and Management*, p. 14, 2012.

[35] A. Uhde, "Wetland dynamics of seasonally flooded forest in the upper amazon," Sep. 2021.

[36] Agéncia Nacional de Águas, "Hidroweb, séries históricas," data retrieved from http://www.snirh.gov.br/hidroweb/serieshistoricas on 03/08/2020.

[37] P. A. Townsend, "Relationships between forest structure and the detection of flood inundation in forested wetlands using C-band SAR," *International Journal of Remote Sensing*, vol. 23, no. 3, pp. 443–460, Jan. 2002.

[38] M. Gupta, A. Sharma, and B. Kartikeyan, "Evaluation of RISAT-1 SAR radiometric calibration using extended amazon rainforest," *Journal of the Indian Society of Remote Sensing*, vol. 45, no. 2, pp. 195–207, Apr. 2017.

[39] J. Bezanson, A. Edelman, S. Karpinski, and V. B. Shah, "Julia: A fresh approach to numerical computing," *SIAM Review*, vol. 59, no. 1, pp. 65–98, 2017. [Online]. Available: https://epubs.siam.org/doi/10.1137/141000671

[40] M. D. Mahecha, F. Gans, G. Brandt, R. Christiansen, S. E. Cornell, N. Fomferra, G. Kraemer, J. Peters, P. Bodesheim, G. Camps-Valls, J. F. Donges, W. Dorigo, L. Estupiñan-Suarez, V. H. Gutierrez-Velez, M. Gutwin, M. Jung, M. C. Londoño, D. G. Miralles, P. Papastefanou, and M. Reichstein, "Earth system data cubes unravel global multivariate dynamics." [Online]. Available: https://www.earth-syst-dynam-discuss.net/esd-2019-62/

[41] QGIS Development Team, *QGIS Geographic Information System*, QGIS Association, 2023. [Online]. Available: https://www.qgis.org

[42] S. Danisch and J. Krumbiegel, "Makie.jl: Flexible high-performance data visualization for julia," *Journal of Open Source Software*, vol. 6, no. 65, p. 3349, 2021. [Online]. Available: https://doi.org/10.21105/joss.03349